

# High-energy-density-physics measurements in implosions using Bayesian inference

J.J. Ruby,<sup>1, a)</sup> J.A. Gaffney,<sup>2</sup> J.R. Rygg,<sup>1, b)</sup> Y. Ping,<sup>2</sup> and G.W. Collins<sup>1, b)</sup>

<sup>1)</sup>*Department of Physics and Astronomy, and Laboratory for Laser Energetics, University of Rochester, Rochester, New York, 14627, USA*

<sup>2)</sup>*Lawrence Livermore National Laboratory, Livermore, California, 94550, USA*

(Dated: 25 February 2021)

Convergent high-energy-density (HED) experimental platforms are used to study matter under some of the most extreme conditions that can be produced on Earth, comparable to the interior of stars. There are many challenges in using these systems for fundamental measurements currently being addressed by new analysis methods, such as the combination of a reduced physics model and Bayesian inference, allowing a self-consistent inference of physical quantities with a robust error analysis. These methods in combination with simple (as compared to inertial confinement fusion implosions) implosion platforms, which can be modified to show sensitivity to different physical mechanisms of interest, are used to study the physical properties of matter under extreme conditions. This work discusses a subset of implosion targets for studying opacity effects, electron-ion equilibration, and thermal conductivity and, as an example, a system consisting of a thick-shelled, gas-filled laser-direct-drive implosion is used to show how a reduced model and Bayesian inference can help inform experimental design decisions such as diagnostic choice. It is shown that for this system that a combination of neutron and x-ray self-emission diagnostics is critical for constraining the details of the thermodynamic states in the system and that the conductivity exponent in a Spitzer like framework can be constrained to the 30% level in deuterium at gigabar conditions. This process can be applied to many HED systems to make underlying model assumptions explicit and facilitate experimental design and analysis.

## I. INTRODUCTION

Laser-driven implosion experiments are motivated by many factors including the pursuit of fusion energy<sup>1,2</sup>, x-ray<sup>3-5</sup>, neutron<sup>6</sup>, or charged-particle<sup>7,8</sup> source development, and the generation of unique conditions leading to interesting physical phenomena<sup>9,10</sup>. While much development has occurred in the application of implosions for inertial confinement fusion (ICF) and for source development, their use for fundamental measurements poses a different set of challenges requiring novel efforts to develop platforms. Some of these challenges include dealing with integrated measurements, gradients in space and time, and computational-intensive high-dimensional models used to describe the systems.

A key feature of implosion experiments is the lack of diagnostic access available to probe the experiment. Most electromagnetic probes are unable to propagate through even the outermost plasma conditions of the targets<sup>11</sup> around the entirety of the target. A noted exception are probes that use photon energies above a few keV which, along with high-energy particle probes<sup>7</sup> are one of the few ways to probe an implosion in situ<sup>12-14</sup>. The primary method of acquiring data on implosion experiments is by measuring the self-emission that is generated by hot-dense plasma states that are created. The two primary quantities generated include x-ray emission energetic enough to escape the target (of order a few keV) and nuclear fusion products, most commonly neutrons from either deuterium tritium fusion or deuterium deuterium fusion.

The production of these quantities depend on the thermodynamic states created throughout the implosion, which is an inherently dynamic process leading to gradients in space and time. The thermodynamic conditions are determined through a complicated mixing of energy transport mechanisms such as hydrodynamics, radiation transport, thermal conduction, particle equilibration, etc. Integrated measurements, the observation of quantities determined by the complex mixing of physical processes, prevent a simple interpretation but conversely they are rich in information content and can be used to gain understanding of the underlying processes.

Typically implosion experiments are modeled using sophisticated radiation hydrodynamics codes<sup>15,16</sup> that are computationally intensive, both in CPU hours and memory requirements<sup>17</sup>. Although able to match the results of experiments post-fact, there is often degeneracy in code inputs, preventing a unique conclusion and the codes generally lack predictive power for future experiments<sup>18,19</sup>.

In order to use implosions experiments to understand physical processes at extreme conditions, it is critical to both design experiments that emphasize some subset of the relevant quantities and also understand how to extract as much information as possible from the implosion, such as with self-emission measurements. This work uses a reduced physics model that is fully constrained by experimental measurements to describe implosions designed to measure physical states and processes, rather than fusion performance or source development.

Using radiation hydrodynamics simulations and synthetic diagnostics, a detailed example of how a reduced model for a thick shell gas filled implosion together with Bayesian inference determine the underlying physical states and processes of such integrated implosions.

---

<sup>a)</sup>Electronic mail: jruby@lle.rochester.edu.

<sup>b)</sup>Also at Mechanical Engineering Department, University of Rochester, Rochester, New York, 14627, USA

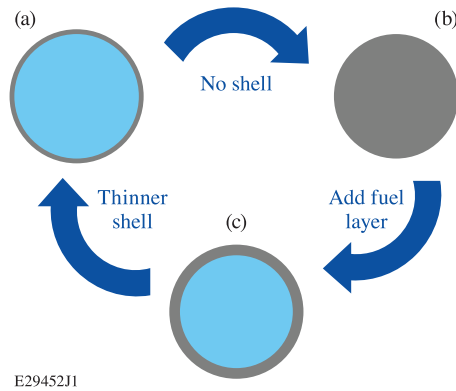


FIG. 1. A representation of the targets discussed within the text, (a) a gas filled thin shell, (b) a solid density sphere, and (c) a gas filled thick shell. Changing the thickness of the shell material moves the experiment between the compressive regime (b) and the shock dominated regime (a) and (c).

## II. ACCESSING DIFFERENT PHYSICS REGIMES THROUGH EXPERIMENTAL DESIGN

The design space of laser-driven implosions is expansive, consisting of target materials, layer thicknesses, laser pulse designs and target scales, that even when accounting for engineering constraints leads to an effectively infinite design space. Even the subspace of "hot-spot ignition"<sup>20,21</sup> targets that (broadly) consist of a CH outer shell layer, a solid DT ice layer, and DT gas, there are enough design parameters to make optimization for a particular metric, such as neutron yield, difficult<sup>18,19,22</sup>, a well-studied issue in the ICF community. In this work a narrow subspace is used as an example of how design changes can move experiments between different physical regimes. A list of common design parameters includes both laser drive conditions, such as total energy, pulse shape, and beam spot size, and target design, such as shell material, diameter, aspect ratio (shell thickness), fill material, and fill pressure, not to mention design differences that differ between direct-drive<sup>21</sup> and indirect-drive experiments<sup>20</sup> such as choice of hohlraum material and shape. Here direct drive experiments are considered with super-Gaussian spatial and temporal laser profiles, and targets that consist of plastic (CH or CD) and deuterium fill (where appropriate) with a fixed outer diameter. The target parameter that is varied is the thickness of the shell or the aspect ratio between the inner cavity and the shell, which moves the experiment through different regimes of energy transport.

The targets considered here can be broadly split into two defining groups, described by the mechanism of energy transport that dominates the implosion. The first group are shock-dominated targets in which the energy transport is dictated by the transit of a single spherical shock. Here the shock initially converges, compressing the target material that begins to flow inwards, upon reaching the target center, it rebounds, re-shocking the inflowing material. A key characteristic of

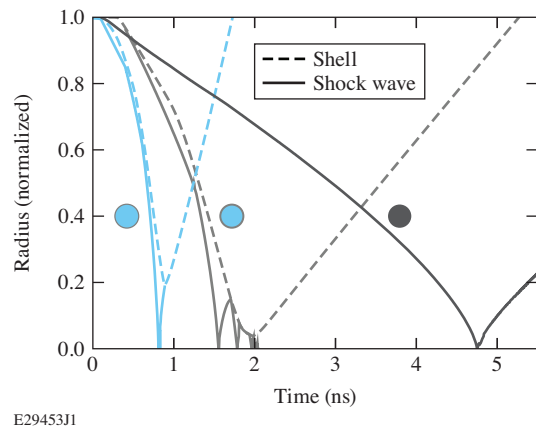


FIG. 2. The shock trajectory (solid lines) and inner shell surface trajectory (dashed lines) for the targets shown in Fig. 1. Target (a) is shown in blue where the shock moves in, rebounds, hits the shell and reverses the shell trajectory, while the shock in target (c), shown in grey, reverberates off the converging shell and undergoes multiple passes through the gas leading to an isobaric hot spot. Target (b), shown in dark grey, has the same dynamics as target (a), a single converging shock wave, but does not feature any shell since it is a single material target. Each trajectory is labelled with the corresponding representation from Fig. 1.

these systems is that after the shock rebounds and passes back through the material the flow of material is outwards leading to decompression. These targets have strong gradients in both space and time. The gradients in temperature, for examples, result in temporally peaked x-ray emission. There is a self-similar semi-analytic model developed by Guderley that can be used to describe these types of implosions<sup>23</sup>.

The second group of targets are compression-dominated targets in which the energy transport is dictated by a massive shell that compresses and inertially confines an inner fuel. These systems also feature a strong converging shock wave that rebounds at the center of the target but when the rebound the shock wave interacts with the massive converging shell of mass, this shell continues inwards leading to shock reverberations and further compression of the fuel. Standard ICF targets fall into this category and there are a number of reduced models developed to describe the behavior<sup>24-26</sup> such as those characterized by a fuel with no spatial pressure gradients (isobaric). Section III uses a compression dominated target as an example to show the utility of using Bayesian inference in combination with a reduced physics model.

Fig. 1 shows a cartoon depiction of these targets, where (A) and (B) are shock dominated and (C) is compression dominated. Target (A) is a very thin-shelled capsule filled with gas density fuel, which is shock dominated as long as the shell mass is low enough to diverge after interaction with the rebounding shock wave, target (B) is a solid density sphere of uniform material which can be thought of as having either no shell or shell thickness equal to the target radius (no fuel), and target (C) is a thick-shell of material with a gas density fuel that is inertially confined by the converging shell.

Fig. 2 shows shock trajectories (solid lines) for targets (A),

(B), and (C) (blue, red, black respectively) and shell trajectories (dashed lines) for targets (A) and (B) (blue and red respectively) all derived from 1-D hydrodynamics simulations. The shock in both (A) and (B) can be seen to converge, rebound, and diverge [with the shell diverging upon interaction with the shock in (A)] and the only difference between these two is the time-scale in which this process happens. The shock travels significantly faster in (A) since the density is over 2 orders of magnitude lower than in (B). In (C) the shock also converges and rebounds, but reflects off of the converging shell and rebounds multiple times while the shell continues to converge, leading to the isobaric hot spot.

In Secs. II A and II B the different physical mechanisms that dominate the energy transport in these regimes and how target designs can affect these mechanisms will be discussed. In addition the change in observable quantities, namely neutron and x-ray self emission, due to the different mechanisms are considered.

### A. Shock-dominated targets

Within shock dominated targets the initial density of the bulk target material is a design parameter that has a significant effect on physical mechanisms of energy transport. In the examples from Figs. 1 and 2, two extremes are given with regard to initial density, one being a thin-shelled target where the bulk target composition is gas density ( $3 \text{ mg/cm}^3$ ) and the other being a fully solid density target ( $1 \text{ g/cm}^3$ ). Recent developments in the construction of foam targets<sup>27</sup> make it possible to achieve a target with a uniform initial density between these two examples.

Since the shock is the primary means that energy is transported through the target, the trajectory and strength of this shock is critical in determining the assembly of the thermodynamic states that exist in these targets. The propagation of the shock is largely determined by the equation of state (EOS) of the material within which the shock propagates. Radiography has been used to map the shock trajectory and measure the EOS of materials<sup>9,10</sup>. These measurements become increasingly difficult as the initial density of the material decreases, due to decreased absorption of the x-ray probes used. In the limit of the gaseous targets the EOS is widely considered to be that of an ideal gas due to the high temperatures and low densities considered ( $\approx$  a few keV and  $\approx$  tens  $\text{mg/cm}^3$ ), although the equation of state of materials at these conditions has not been directly measured. Due to these high temperatures and low densities electron-ion equilibration becomes an important mechanism to consider for the distribution of energy in the systems with low initial densities.

At the conditions being considered, the material experiences some level of ionization and the shock preferentially deposits energy into the ions over the free electrons due to their larger masses<sup>28</sup>. The ion-ion and electron-electron collisional rates are sufficiently high that the individual species quickly equilibrate when compared to the dynamical time scale of the system ( $\approx 10$  ps) but, due to the mismatch in mass, the electron-ion collision timescale ( $\tau_{ei}$ ) is not necessarily short

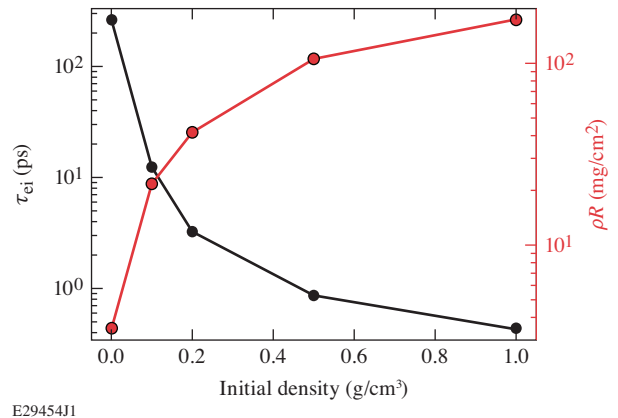


FIG. 3. Electron-ion coupling constant (calculated according to Spitzer<sup>29</sup>), shown in black, and the areal density, shown in red, for various initial densities in the shock driven systems for temperature and density conditions around the time of peak self-emission. At lower densities the dynamical timescales, 10s of ps, are equal to or shorter than the equilibration rate which plays a crucial role in generated emission. At high initial densities the equilibration rate is sufficiently fast that it does not factor into observations but the areal density is large enough that scattering and absorption of emission is an important consideration for observations.

enough to for the species to equilibrate in the shock-driven systems. Figure 3 shows the electron-ion coupling time calculated according to Spitzer's formalism<sup>29</sup> for shock-driven systems subject to the same laser pulse but with different initial densities of the bulk material. The coupling time of the low-density targets is much greater than the dynamic time scales involved, ensuring the the equilibration has significant leverage on observable quantities such as neutron and x-ray production (through the ion temperature and electron temperature, respectively). As the initial density increases, the final target densities increase and the final temperature decreases, leading to much faster equilibration rates and by roughly half-solid density ( $\approx 0.5 \text{ g/cm}^3$ ) the species are fully equilibrated over the relevant time scales of the experiment (the duration of emission).

The targets that are less sensitive to electron-ion equilibration are more sensitive to the absorption and scattering of both x-rays and neutrons produced from the shock collapse. Figure 3 shows the areal density ( $\rho R$ ) at the time of peak self-emission for the shock-dominated targets as a function of initial target density. As the  $\rho R$  increases, the self-emission, which is created in the highest temperature states at the center of the target, is subject to increased scattering and absorption due to the remaining material in the outer parts of the target. As an example, carbon (a commonly used component in shock driven targets<sup>9,10,30</sup>) has a cold opacity of  $19.12 \text{ cm}^2 \text{ g}^{-1}$  for photon energies of 5 keV, an x-ray energy that many diagnostics are sensitive to, meaning that the most dense target from Fig. 3 has a transmission of  $< 4\%$  at 5 keV while the least dense target has a transmission of  $> 93\%$ . In these systems the opacity is likely not equal to the well-characterized cold-opacity, but rather the bulk of absorption occurs in ma-

terial that is at or above solid density and tens to hundreds of eV temperatures, a range of conditions known as warm dense matter, where the material properties, including opacity<sup>32,33</sup>, are not well understood<sup>34</sup>. Targets with higher  $\rho R$  demonstrate significant absorption of x-rays and are highly sensitive to the opacity of the bulk material.

## B. Compression-dominated targets

Targets with significant compression from the inertia of the shell material are well studied<sup>20,35</sup>, primarily due to efforts made in ICF and in particular, producing experiments that generate significant amounts of fusion energy<sup>21,26,36</sup>. In this work, a subset of compressive implosions is considered, specifically with the goal of being as robust against 3-D effects as possible and therefore explicable through the lens of a radially symmetric 1-D model. The highest-performing ICF implosions require high implosion velocities and low shell masses, leading to high convergence and significant perturbation growth<sup>16</sup>, while the implosions discussed here use thicker shells and lower implosion velocities and higher entropy states (driven by a single strong shock) in order to emphasize the 1-D symmetry of the system.

The primary mode of energy transfer into the fuel in these experiments comes from kinetic energy transfer from the high inertia shell as it slows down and compresses the fuel. Unlike the shock systems, where the states are established by an evolving converging and diverging shock wave, the dynamics of energy transfer in the compressive regime make electronic thermal conductivity and radiative energy losses important factors in the overall evolution of the states that are created<sup>20,24,25,35,37</sup> implying that the measurements from implosion platforms are sensitive to the details of thermal conductivity and radiative properties. Although the targets discussed here firmly exist in either the shock or compression-dominated regime there is no binary transition between the two but rather a spectrum of targets that share the qualities (and complexities) of both types of targets.

The following section. III will give an example of a reduced-physics model for a compressive hot spot with temperature profiles determined by the details of the thermal conductivity of the fuel.

## III. BAYESIAN INFERENCE FOR EXPERIMENTAL DECISION MAKING

The combination of reduced-physics models<sup>38</sup> and Bayesian inference are a powerful tools when considering the integrated nature of self-emission measurements that come from implosion experiments. This process has already been successfully applied to a shock-dominated system<sup>38,39</sup> to understand the energy transfer and pressures during the experiment. The primary benefit of using Bayesian inference for parameter estimation in HED experiments rather than other methods is the full construction of the posterior probability distributions with no assumptions about the shape

of the posterior distributions, unlike error estimates in most other inference techniques such as least-squares fitting. A deeper discussion about the benefits of Bayesian inference in these systems can be found elsewhere<sup>38</sup>.

Here a reduced-physics model describing the pressure, temperature, and density inside of a compression-dominated hot spot is formulated and constrained using synthetic data generated by the 1-D hydrodynamics code *LILAC*<sup>15</sup>.

### A. Reduced model for a hot spot

In the presented model, which is heavily influenced by reduced hot spot models in the literature<sup>20,24,25,35,37</sup>, the thermodynamic states of the hot spot are established through energy balance and conservation equations starting with a time-dependent parameterization of the hot spot energy, given by a Gaussian function

$$E(t) = E_0 e^{-\frac{(t-t_E)^2}{2\sigma_E^2}} \quad (1)$$

where  $E_0$ ,  $t_E$ , and  $\sigma_E$  are the peak internal energy, time of peak energy, and width of the temporal energy profile, respectively. Each of these is a free parameter of the model.

The radial extent of the hot spot,  $R$ , is defined by a trajectory of constant acceleration,

$$R(t) = R_0 + v_0 t + \frac{1}{2} a_0 t^2 \quad (2)$$

and defines a time dependent hot spot volume

$$V(t) = \frac{4}{3} \pi R(t)^3. \quad (3)$$

The energy and volume then give the pressure

$$P(t) = \frac{E(t)}{c_V V(t)}, \quad (4)$$

assuming an ideal gas equation of state with a specific heat at constant volume,  $c_V$ .

A two-temperature fluid is assumed, with the electron temperature,  $T_e$ , and ion temperature  $T_i$  both having the same self-similar temperature profiles given by

$$T_{e,i}(r,t) = T_{e,i}^0 T_r(r/R_{HS}) \quad (5)$$

where  $T_{e,i}^0$  is the (electron,ion) temperature at  $r = 0$  and  $R_{HS}$  is the boundary of the hot spot. Following from conservation of mass and an ideal gas equation of state we get the relationship

$$\frac{\dot{M}}{M} = \frac{\dot{E}}{E} - \frac{\dot{T}^0}{T^0}, \quad (6)$$

where  $T^0 = \bar{Z} T_e^0 + T_i^0$  and  $\bar{Z}$  is the average ionization state,  $Z = 1$  in this case considering fully ionized hydrogen. Since the hot spot is defined by the fuel it is fixed mass so  $\dot{M} = 0$  and

$$\frac{\dot{E}}{E} = \frac{\dot{T}^0}{T^0}. \quad (7)$$

Integrating Eq. (7), with the initial condition  $T^0(t = t_0) = T^{00}$  gives  $T^0(t) = \bar{Z}T_e^0(t) + T_i^0(t)$  but the individual central temperatures for electrons and ions are still unknown. The ideal equation of state allows the radial density distribution to be constructed from the radial temperature distributions,

$$\rho(r) = \frac{\bar{A}P}{N_A \bar{Z}T_e(r) + T_i(r)} \quad (8)$$

where  $\bar{A}$  is the average atomic mass and  $N_A$  is Avogadro's number. The radial temperature profiles  $T_{e,i}(r)$  follow from solving the two temperature heat conduction equation,

$$\frac{c_P P}{\bar{Z}T_e + T_i} \left( \bar{Z} \frac{\partial T_e}{\partial t} + \frac{\partial T_i}{\partial t} \right) = \frac{1}{r^2} \frac{\partial}{\partial r} \kappa_e r^2 \frac{\partial T_e}{\partial r} + \frac{1}{r^2} \frac{\partial}{\partial r} \kappa_i r^2 \frac{\partial T_i}{\partial r} \quad (9)$$

where  $\kappa_{e,i}$  is the (electron,ion) thermal conductivity which combine to give the total conductivity,  $\kappa_0$  as

$$\kappa = \bar{Z}\kappa_e + \kappa_i \quad (10)$$

and the total conductivity is assumed to be of the form

$$\kappa = \kappa_0 \left( \frac{\rho}{\rho_0} \right)^a \left( \frac{T}{T_0} \right)^b \quad (11)$$

where  $a$  and  $b$  are the conductivity exponents as established in Spitzer<sup>29</sup>. Combining Eqs. (8) - (10) and separating the temporal and spatial components leads to a coupled equation for the radial temperature profile,  $T_r$ , and the central temperatures,  $T_e^0$  and  $T_i^0$ ,

$$\begin{aligned} \frac{\partial}{\partial t} (\bar{Z}T_e^0 + T_i^0) = \\ \frac{\lambda}{1 + \bar{Z} \rho_0^a T_0^b \gamma} \left( \frac{\bar{A}}{N_A c_V} \right)^a \left( \frac{E}{V} \right)^{a-1} \frac{\bar{Z}(T_e^0)^{1+b} + (T_i^0)^{1+b}}{(\bar{Z}T_e^0 + T_i^0)^{a-1}} \end{aligned} \quad (12)$$

with

$$\lambda = \frac{1}{r^2} \frac{\partial}{\partial r} r^2 T_r^{b-a} \frac{\partial T_r}{\partial r}. \quad (13)$$

Using the boundary conditions  $T_r(r = 0) = 1$  and  $T_r(r = R_{HS}) = \eta$  ( $\eta < 1$ ) the radial profile can be found as

$$T_r = \left[ 1 - \left( \frac{r}{R_{HS}} \right)^2 (1 - \eta^{1+b-a}) \right]^{\frac{1}{1+b-a}}. \quad (14)$$

Now since  $T^0(t)$  is known along with the radial terms for  $T_{e,i}(r,t)$  all that remains is a relationship between  $T_i^0$  and  $T_e^0$  to close the system. This relationship can take any form, including the simplest case where  $T_e^0 = T_i^0$ , here the relationship

$$T_e^0 = T_i^0 - D e^{-t/\tau} \quad (15)$$

is used, where  $D$  and  $\tau$  are parameters of the model relating to the initial difference in the electron and ion temperatures and

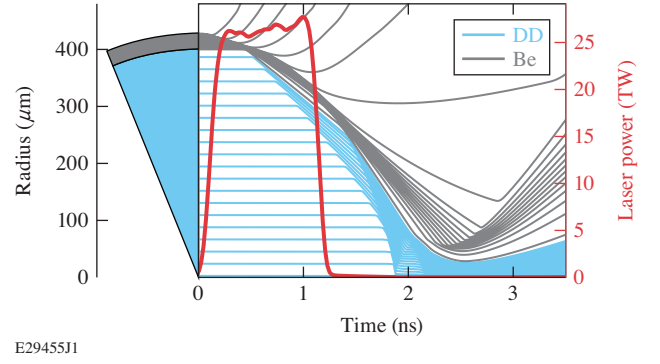


FIG. 4. Lagrangian particle trajectories for the shell material (grey) and gas (blue) in the simulated target. Also shown is the laser pulse (red) used to drive the target. On the left a wedge of the target is shown for context.

the rate at which they equilibrate, related to but not equal to the electron-ion coupling time scale<sup>28,29,35</sup>.

At this point all of the thermodynamic variables can be constructed in space and time giving  $P(t)$ ,  $V(t)$ ,  $T_e(r,t)$ ,  $T_i(r,t)$ , and  $\rho(r,t)$ . The quantities required to close the model are  $E(t)$ ,  $R_{HS}(t)$ ,  $T^{00}$ ,  $\eta(t)$ ,  $a$ ,  $b$ ,  $c_V$ ,  $D$ , and  $\tau$ . It should be noted that the boundary temperature  $\eta(t)$  can be independent for both the electrons and ions, but in this work will be taken as the same value for the electrons and ions.

An obvious extension of this model is the inclusion of parameters that describe the shell, which would have kinetic energy related to the internal energy of the hot spot changing the parameterization of the trajectory of the hot spot size and which would contribute to the hot spot mass through conductive ablation, an important mechanism in ignition-scale implosions<sup>24,37</sup>. In this case the situation is simplified by considering the hot spot as an independent system that is not necessarily closed, i.e. energy need not be conserved within the system.

## B. LILAC simulation and synthetic data used for comparison

It is important to validate the reduced model against a more complete physics simulation<sup>38</sup>, in this case the 1-D Lagrangian hydrodynamics code *LILAC*<sup>15</sup> is used. The simulated system includes a 30- $\mu\text{m}$  beryllium shell filled with 15 atm. of  $\text{D}_2$  gas and has an outer diameter of 860- $\mu\text{m}$ . This target is driven with 27 kJ of UV laser light in a 1-ns square pulse. The laser pulse and target are shown in Fig. 4 along with Lagrangian zone trajectories for the fuel and shell.

The simulation output includes the thermodynamic states (temperature, density, pressure, etc.) in each zone, and these are used to calculate the amount of x-ray self-emission, assuming a Bremsstrahlung emissivity<sup>35,40</sup>, and neutron self-emission, calculated from D-D fusion reactivities<sup>41</sup>. These quantities are then used to produce synthetic measurements based on typical implosion diagnostics, in particular time-gated radial x-ray profile measurements (such as would be measured by an x-ray framing camera<sup>42</sup>), time-resolved x-ray

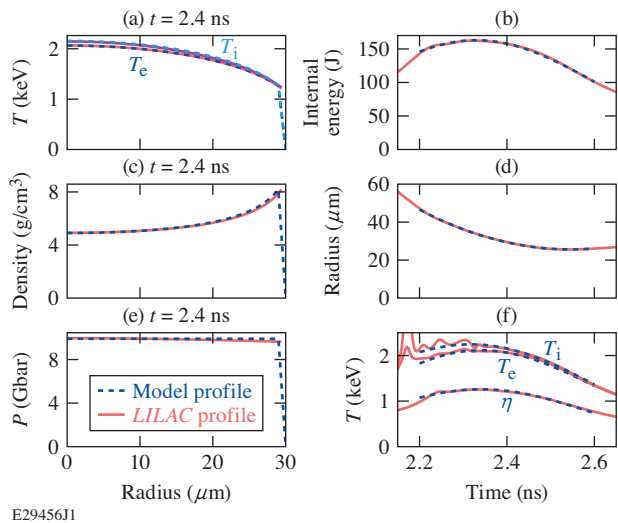


FIG. 5. A comparison of the simulated profiles (solid red) and profiles from a well fitting set of parameters (dashed blue) for the reduced model; profiles shown are both in space (left) and time (right). This shows that the reduced model is able to recover the profiles from LILAC in space and time for all of the relevant thermodynamic quantities including (a) the electron and ion temperatures, (b) the internal energy in the hotspot, (c) the mass density, (d) the hotspot radius, (e) the pressure, and (f) the electron and ion temperatures at the boundaries. This does not guarantee that any given set of measurements is enough to recover the parameters, but does verify the utility of the reduced model in describing the full system.

emission with multiple different spectral channels (as would be measure by multiple diagnostics<sup>43–45</sup>, the temporal history of the neutron production, neutron spectrum, and neutron yield, all of which are standard measurements in ICF experiments<sup>46,47</sup>. These are "idealized" synthetic data, meaning an attempt was made to account for the instrument response functions for each measurement and typical uncertainties were used for each but no attempt was made at simulating typical background signals or other noise sources associated with each measurement. Additionally, the spectral and temporal channels were chosen such that sources of emission other than the hot spot, such as xrays from the shell material either during the laser drive or when the hot spot is assembled, are ignored. This is a plausible set of measurements, but care must be taken to determine the exact photometrics of these measurements prior to performing an experiment.

The details of this target were chosen to promote as uniform an implosion as possible. A thick shell driven with a single strong shock is a "high-adiabat"<sup>2,24,35</sup> implosion, robust to hydrodynamic perturbations.

The philosophy proposed in this work is to investigate the simplest experimental system possible that still contains the physics of interest, so the simplest reduced model can be used to infer quantities and then complexity can be added to the model allowing, more-interesting systems to be investigated. This is a bottom-up approach to the problem and is not currently widely used but the current efforts<sup>19,22,48</sup> in ICF have seen progress using a top-down approach leveraging the most-

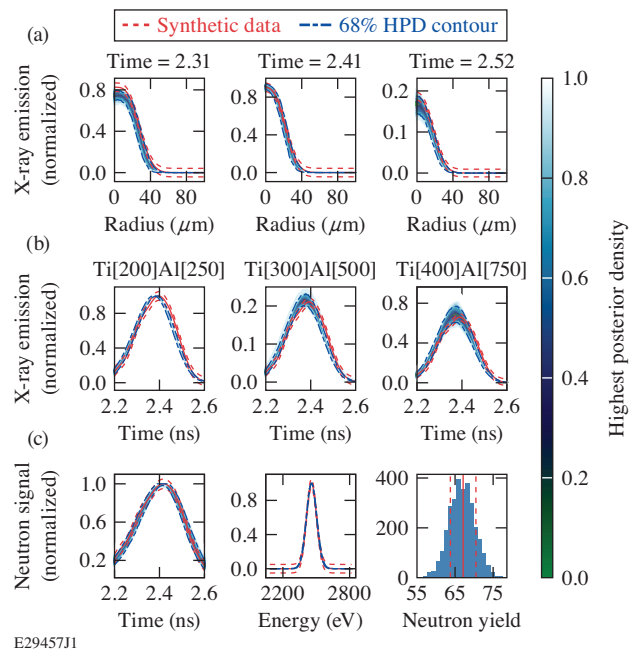


FIG. 6. A comparison of the predicted distributions (color map) for observations from Bayesian inference and the synthetic data generated (red solid) with normally distributed errors (dashed shows  $1-\sigma$ ), for (a) radial x-ray profiles at 3 (out of 16) times, (b) x-ray temporal histories in 3 different spectral channels, and (c) the neutron burn rate, spectrum, and yield (left to right). The inferred quantities are shown with a highest posterior density on the color scale. The inferred distributions from the model are able to reasonably reproduce the data across all measurements.

complete physics models to understand the experimental landscape and increase performance. The goal in this work is not to make "better" implosions with regards to ICF performance but to design an implosion that can plausibly be meaningfully described by a reduced model.

### C. Insight from Bayesian inference using reduced model and synthetic data

Advanced statistical techniques are beginning to be regularly used for the design of implosion experiments, in particular using large numbers of simulations to optimize for a particular performance metric<sup>17,18,49</sup>. This work uses Bayesian inference to understand how well the underlying quantities of a simulation can be reconstructed based on a typical set of measurements. There are three key details that determine the efficacy of this process: (1) The full-physics model being used (in this case a 1-D radiation-hydrodynamics code) is believed to reasonably represent the experimental system; (2) The reduced-physics model accurately represents quantities of interest from the full physics model; and (3) the reduced-physics model can be constrained by the available measurements.

The first point is likely the most challenging to be fully convinced of and requires additional effort beyond what is pre-

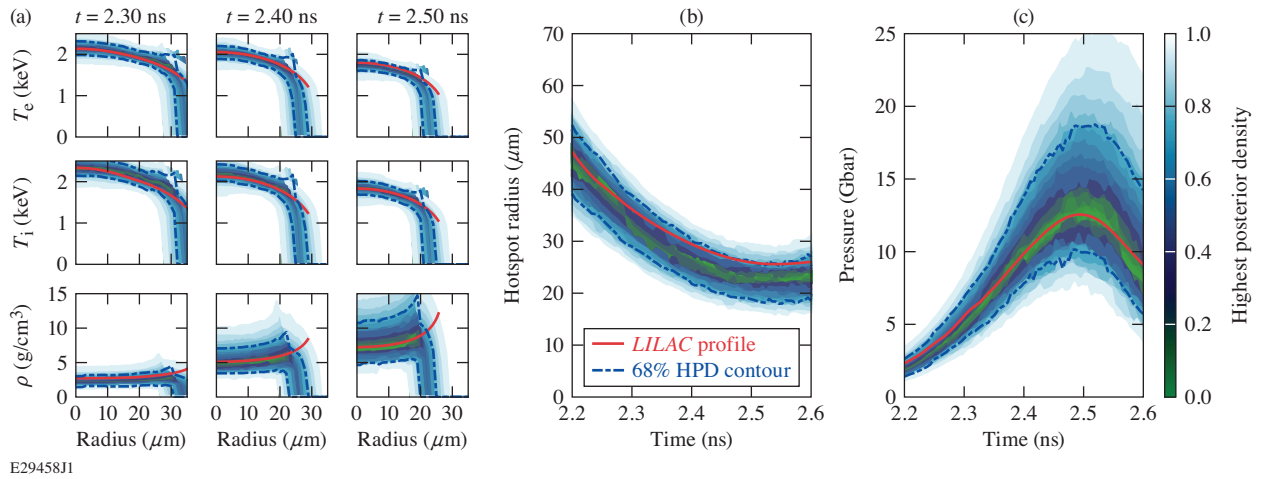


FIG. 7. A comparison between the inferred profiles from the reduced model, again showing highest posterior densities in the color map with green representing the most likely (median) prediction, and underlying profiles from the simulation (red) for (a) the radial dependence of electron temperature, ion temperature, and density at 3 different times, (b) the temporal history of the hot spot radius, and (c) the temporal profile of the hot spot pressure. The inferred quantities do an excellent job recovering the underlying profiles with the exception of the hot spot radius, which is under predicted throughout, leading to the truncation of the radial profiles in (a).

sented here. The full-physics model need not be predictive of experiments but it must contain the essential physics of the experiment. For example, if there was significant asymmetry observed in an experiment, it is obvious that a 1-D model will not be sufficient to describe the system and a 2-D or 3-D simulation would be more appropriate along with a more sophisticated reduced model. The benefit of the reduced model over the full physics models is that they recast the full simulation parameter space, which has some large dimensionality dependent on the detailed physics in the model, into the reduced model parameter space, which in this case has 15 parameters making it possible to run a full Monte Carlo sampling in tens of CPU hours rather than tens of millions of CPU hours<sup>17,19,50</sup> that a full scale hydrodynamics simulation would require.

The second point is addressed by seeing if there are a set of reduced model parameters that are able to reproduce profiles from the full simulation. Figure 5 shows a comparison between the reduced model profiles (dashed blue lines) and the profiles from LILAC (solid red lines) for a number of quantities in space and time. There is very good agreement between the reduced model (given a particular choice of parameters) and LILAC across space and time for all of the underlying quantities of interest. This is evidence that the reduced model captures the essential physics necessary to describe the evolution of the hot spot around the time of peak emission ( $\approx 2.4$  ns in LILAC).

The third point is addressed through the use of Bayesian inference<sup>38</sup>. Assuming that the system under consideration is well described by the full-physics model (first point), and the reduced-physics model adequately represents the pertinent quantities from the full model (second point), the question remains as to whether the reduced model can be constrained by observations that are readily available or, if not, what measurements are required to constrain the model.

Here the simulated measurements, as mentioned in Sec.

III B, include framing camera data sampled at 16 different times, temporal x-ray history in three different spectral channels above  $\approx 15$  keV, the temporal history of neutron emission, the thermal neutron spectrum, and the total neutron yield. Figure 6 shows the predicted distributions for a set of the simulated measurements based on a Monte Carlo sampling of the reduced model. The model is able to reproduce all of the measurements shown within the 68.7% credible intervals (shown by the blue dashed-dotted lines). The profiles that result from the sampling shown in Fig. 6 are shown in Fig. 7 along with the underlying simulation profiles. The predicted profiles from the reduced model show excellent agreement with the "true" profiles that from the underlying simulation for the electron and ion temperatures, density, and pressure in space and time. The exception is the hot-spot radius as a function of time, which is under-predicted for all times. This leads to the truncation of the radial profiles seen in Fig. 7(a). It is clear that, with respect to the third point above, the set of synthetic measurements presented here is enough to constrain the reduced model and reproduce the underlying profiles of interest.

An interesting next step is to investigate how the predictions vary with or without different measurements. This is presented in Fig. 8, where the results for the central electron and ion temperatures, central density, and hot-spot pressure are compared to the underlying simulation (red points) for three different times. Each box represents a different data set used, including the full data (green), excluding the neutron spectrum (cyan), excluding the spatial x-rays (blue), excluding the temporal x-rays (navy), and using a known hot spot radius for all times (purple). Leaving out the neutron spectrum has a minimal impact on the inferred profiles, meaning that the information contained in the neutron spectrum (in this particular simulated implosion) is redundant with the other measurements. The neutron spectrum is generally considered

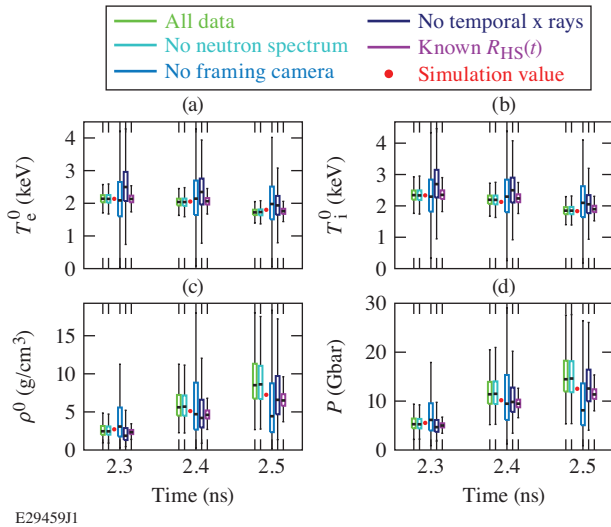


FIG. 8. A boxplot comparing the inferred thermodynamic parameters from the reduced model and the underlying values from the simulation (red) for (a) the central electron temperature, (b) central ion temperature, (c) central density, and (d) pressure at 3 different times. The different color boxes represent the results inferred using different datasets including the full data (green), excluding the neutron spectrum (cyan), excluding the x-ray radial data (blue), excluding the x-ray temporal data (navy), and using a known hot spot radius for all times (purple). The boxes represent the upper and lower quartiles of the inferred distributions and the bars show the full extent of the distributions.

constraining on the ion-temperature of the system<sup>51,52</sup> but the information is likely redundant with the neutron yield (which is very sensitive to ion temperature through the reactivity) and the x-ray spectral information contained in the temporal x-ray history. Additionally the neutron spectrum is integrated over space and time leaving only a single integrated measurement of the temperature that is not very constraining of the temporal and spatial evolution of the temperatures. Conversely excluding either x-ray measurement results in a significant increase in uncertainty for the profiles, beyond the point of usefulness in most cases. The radial information contained in synthetic framing camera data is critical to setting the states within the hot spot and the temporal x-ray history helps break the degeneracy that exists within the neutron dataset. Finally, a dataset with a known hot spot radius significantly reduces the uncertainty on the inferred densities and pressures, with a much more modest reduction in uncertainty on the temperatures, although it does rectify the early truncation of the profiles seen in Fig. 7.

To demonstrate the degeneracy that arises in model parameters when a measurement is excluded, Fig. 9 (b) and (c) shows the pairwise posterior distributions for the time of peak energy,  $t_E$  and the hot spot radius at  $t_E$ , given by the trajectory parameters  $R_0$ ,  $v_0$ , and  $a_0$  along with histograms of the parameter values in Fig. 9 (a) and (d). The red distribution in (b) includes all of the measurements and the blue distribution in (c) excludes the framing camera measurements. The distribution without the framing camera shows that these two

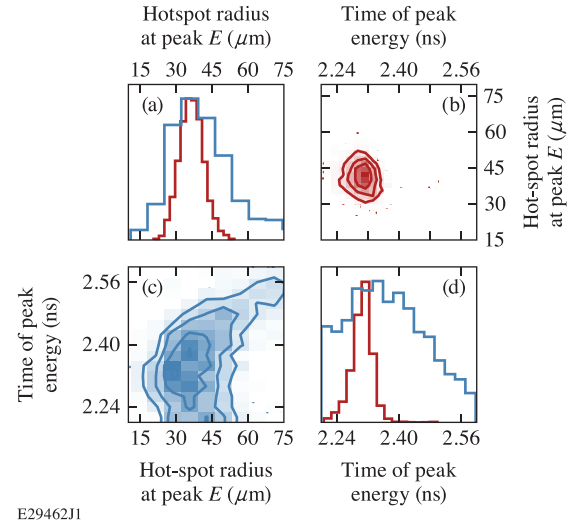


FIG. 9. Pairwise distribution for the time of peak energy,  $t_E$ , and hot spot radius at time of peak energy,  $R_{HS}(t_E)$ , showing (c) their strong correlation without the framing camera data and (b) how the degeneracy is broken when all of the measurements are used. The projected histograms for (a) the radius and (d) the time both show the effect of the using all the data (red) in narrowing the distributions from the case without the framing camera (blue). Note the axes in (b) are transposed from those in (c).

parameters are strongly correlated, with a positive correlation coefficient, leading to very broad posterior distributions for both parameters in (a) and (d). The framing camera breaks this degeneracy resulting in distributions with minimal correlations and much more narrow posterior distributions.

This result may be somewhat surprising because even without the framing camera measurements there is still neutron and x-ray temporal measurements that may be expected to constrain the temporal history of the fuel internal energy, but seemingly do not. The degeneracy exists because both the x-ray and neutron yields depend on the energy of the hot spot and the volume of the hot spot (the energy density) meaning that the peak in emission does correspond to the peak in internal energy, but rather the peak in energy density which depends on the radius and energy and the degeneracy is broken with the time-gated radial measurements of emission from the framing camera.

Finally the ability to extract information about the thermal conductivity is presented in Fig. 10 which shows a boxplot, similar to Fig. 8, but for the conductivity exponent which depends on a combination of the temperature and density dependencies,  $b$  and  $a$ , respectively, following from Eq. 14. Since the temperature profile depends on this combination of parameters, and the emission profiles depend on the temperature profile, it is this quantity that is constrained. The underlying simulation made use of Spitzer conductivities<sup>29</sup>, which have  $a = 0$  and  $b = 2.5$  so the quantity  $(1 + b - a)^{-1} = 0.286$ , shown with the red point in the figure. The conductivity exponent has a modest effect on the temperature profile, and this can be seen here where, despite the temperature profiles being well constrained by the measurements as shown in Fig. 7, the con-

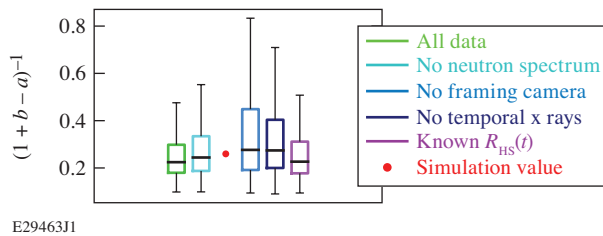


FIG. 10. A boxplot comparing the inferred conductivity exponent from the same data sets in Fig. 8 and the true exponent from the conductivity model used in the *LLAC* simulations ( $0.286$  for  $a = 0$  and  $b = 2.5$ )<sup>29</sup>. Even the models using the most data could only constrain the conductivity profile to within 10s of percent due them measurements being derived from the temperature profiles and the profiles' weak dependence on the conductivity exponent.

ductivity exponent has a fairly broad distribution in the best case resulting in  $0.25 \pm_{0.1}^{0.08}$  (median  $\pm 68.7\%$  highest posterior density interval). The conductivity exponent under these conditions can be constrained at the few tens of percent level, future work is needed to investigate the necessary precision to distinguish between conductivity models and what, if any, additional measurements can produce a tighter constraint on the conductivity.

Important to note is the choice of likelihood function used throughout the Bayesian inference process. In this work a Gaussian likelihood was used, which is most appropriate when considering data with uncorrelated and normally distributed errors. There are many likelihood functions that can be considered and some work has been done within HEDP to explore the effects of different choices<sup>50</sup>. Likelihood functions contribute to the shape of the posterior distributions and therefore can affect the interpretation of uncertainties from the inference process. This is particularly important when considering data with correlated errors such as spectral measurements and imaging data<sup>50</sup>. A major concern is introducing bias into the inferred parameters by way of a poor likelihood choice in combination with a poor choice of model further emphasizing the necessity of doing properly controlled synthetic experiments, as shown here, to ensure that the inferred distributions accurately represent the physical quantities that they represent and that the shape of those distributions present a reasonable picture of uncertainty. Different choice of likelihoods can be used to combat bias introduced by model form error<sup>50</sup> but here preference is given to using a likelihood that most accurately represents the underlying distribution of the experimental data. In either case a rigorous look at synthetic data is a powerful tool in understanding the limitations of both the model and likelihood choices.

#### IV. CONCLUSIONS

Laser-driven implosion experiments can reach a wide variety of interesting high-energy-density conditions and there is great opportunity for discovery in these systems. Basic target design with a simple laser pulse shape is able to transition

between interesting energy regimes — shock dominated and compression dominated — and within those regimes different types of transport physics as able to be emphasized depending on the initial conditions. There are a standard set of measurements able to be made in laser driven implosions and the understanding how the measurements are sensitive to different physical mechanisms is key to understanding the physics and measurements. Reduced models coupled with Bayesian inference give a straightforward way to explicitly state the assumptions of a particular analysis, and understand how the measurements are able to constrain the model of the system.

An example of this process, using a thick shell implosion driven with a square pulse, shows that the thermodynamic profiles (temperature, density, pressure) of the assembled hot spot can be reconstructed in space and time using standard self-emission measurements of x-rays and neutrons. In addition it is shown that the neutron spectrum does not have much leverage on the spatial and temporal profiles of temperature, but time-gated spatial resolved x-rays measurements in combination with time-resolved and spectrally gated x-ray measurements are very constraining when used with neutron burn rate and yield measurements.

This process presents a new modality for experimental design that allows an analysis pipeline to be built and tested prior to an experiment informing both experimental design and diagnostic decisions for the experiment. This process can be expanded to any number of systems and used both in the pursuit of inertial fusion ignition and understanding of fundamental HED physics.

#### ACKNOWLEDGMENTS

This material is based upon work supported by the Department of Energy National Nuclear Security Administration under Award Number DE-NA0003856, the U.S. Department of Energy, Office of Science, Office of Fusion Energy Sciences under Award No. DE-SC001926, the University of Rochester, and the New York State Energy Research and Development Authority. Y. P. acknowledges support from DOE OFES early career program and LLNL LDRD program.

This report was prepared as an account of work sponsored by an agency of the U.S. Government. Neither the U.S. Government nor any agency thereof, nor any of their employees, makes any warranty, express or implied, or assumes any legal liability or responsibility for the accuracy, completeness, or usefulness of any information, apparatus, product, or process disclosed, or represents that its use would not infringe privately owned rights. Reference herein to any specific commercial product, process, or service by trade name, trademark, manufacturer, or otherwise does not necessarily constitute or imply its endorsement, recommendation, or favoring by the U.S. Government or any agency thereof. The views and opinions of authors expressed herein do not necessarily state or reflect those of the U.S. Government or any agency thereof.

Prepared by LLNL under Contract DE-AC52-07NA27344. This document was prepared as an account of work sponsored by an agency of the United States government. Neither the

United States government nor Lawrence Livermore National Security, LLC, nor any of their employees makes any warranty, expressed or implied, or assumes any legal liability or responsibility for the accuracy, completeness, or usefulness of any information, apparatus, product, or process disclosed, or represents that its use would not infringe privately owned rights. Reference herein to any specific commercial product, process, or service by trade name, trademark, manufacturer, or otherwise does not necessarily constitute or imply its endorsement, recommendation, or favoring by the United States government or Lawrence Livermore National Security, LLC. The views and opinions of authors expressed herein do not necessarily state or reflect those of the United States government or Lawrence Livermore National Security, LLC, and shall not be used for advertising or product endorsement purposes. Manuscript number: LLNL-JRNL-816774.

## V. DATA AVAILABILITY

The data that support the findings of this study are available from the corresponding author upon reasonable request.

- <sup>1</sup>E. M. Campbell, V. N. Goncharov, T. C. Sangster, S. P. Regan, P. B. Radha, R. Betti, J. F. Myatt, D. H. Froula, M. J. Rosenberg, I. V. Igumenshchev, W. Seka, A. A. Solodov, A. V. Maximov, J. A. Marozas, T. J. Collins, D. Turnbull, F. J. Marshall, A. Shvydky, J. P. Knauer, R. L. McCrory, A. B. Sefkow, M. Hohenberger, P. A. Michel, T. Chapman, L. Masse, C. Goyon, S. Ross, J. W. Bates, M. Karasik, J. Oh, J. Weaver, A. J. Schmitt, K. Obenschain, S. P. Obenschain, S. Reyes, and B. Van Wronterghem, *Matter and Radiation at Extremes* **2**, 37 (2017).
- <sup>2</sup>O. A. Hurricane, D. A. Callahan, D. T. Casey, P. M. Celliers, C. Cerjan, E. L. Dewald, T. R. Dittrich, T. Döppner, D. E. Hinkel, L. F. Hopkins, J. L. Kline, S. Le Pape, T. Ma, A. G. MacPhee, J. L. Milovich, A. Pak, H. S. Park, P. K. Patel, B. A. Remington, J. D. Salmonson, P. T. Springer, and R. Tommasini, *Nature* **506**, 343 (2014).
- <sup>3</sup>B. Yaakobi, F. J. Marshall, T. R. Boehly, R. P. J. Town, and D. D. Meyerhofer, *Journal of the Optical Society of America B* **20**, 238 (2003).
- <sup>4</sup>F. Coppari, D. B. Thorn, G. E. Kemp, R. S. Craxton, E. M. Garcia, Y. Ping, J. H. Eggert, and M. B. Schneider, *Review of Scientific Instruments* **88** (2017), 10.1063/1.4999649.
- <sup>5</sup>M. C. Jones, D. J. Ampleford, M. E. Cuneo, R. Hohlfelder, C. A. Jennings, D. W. Johnson, B. Jones, M. R. Lopez, J. Macarthur, J. A. Mills, T. Preston, G. A. Rochau, M. Savage, D. Spencer, D. B. Sinars, and J. L. Porter, *Review of Scientific Instruments* **85** (2014), 10.1063/1.4891316.
- <sup>6</sup>G. Ren, J. Yan, J. Liu, K. Lan, Y. H. Chen, W. Y. Huo, Z. Fan, X. Zhang, J. Zheng, Z. Chen, W. Jiang, L. Chen, Q. Tang, Z. Yuan, F. Wang, S. Jiang, Y. Ding, W. Zhang, and X. T. He, *Physical Review Letters* **118**, 1 (2017).
- <sup>7</sup>J. R. Rygg, F. H. Séguin, C. K. Li, J. A. Frenje, M. J. Manuel, R. D. Petrasso, R. Betti, J. A. Delettrez, O. V. Gotchev, J. P. Knauer, D. D. Meyerhofer, F. J. Marshall, C. Stoeckl, and W. Theobald, *Science* **319**, 1223 (2008).
- <sup>8</sup>M. J. Rosenberg, H. G. Rinderknecht, N. M. Hoffman, P. A. Amendt, S. Atzeni, A. B. Zylstra, C. K. Li, F. H. Séguin, H. Sio, M. G. Johnson, J. A. Frenje, R. D. Petrasso, V. Y. Glebov, C. Stoeckl, W. Seka, F. J. Marshall, J. A. Delettrez, T. C. Sangster, R. Betti, V. N. Goncharov, D. D. Meyerhofer, S. Skupsky, C. Bellei, J. Pino, S. C. Wilks, G. Kagan, K. Molvig, and A. Nikroo, *Physical Review Letters* **112**, 1 (2014).
- <sup>9</sup>T. Döppner, D. C. Swift, A. L. Kritcher, B. Bachmann, G. W. Collins, D. A. Chapman, J. Hawreliak, D. Kraus, J. Nilsen, S. Rothman, L. X. Benedict, E. Dewald, D. E. Fratantuono, J. A. Gaffney, S. H. Glenzer, S. Hamel, O. L. Landen, H. J. Lee, S. Lepape, T. Ma, M. J. Macdonald, A. G. MacPhee, D. Milathianaki, M. Millot, P. Neumayer, P. A. Sterne, R. Tommasini, and R. W. Falcone, *Physical Review Letters* **121**, 25001 (2018).
- <sup>10</sup>A. L. Kritcher, D. C. Swift, T. Döppner, B. Bachmann, L. X. Benedict, G. W. Collins, J. L. DuBois, F. Elsner, G. Fontaine, J. A. Gaffney, S. Hamel, A. Lazicki, W. R. Johnson, N. Kostinski, D. Kraus, M. J. MacDonald, B. Maddox, M. E. Martin, P. Neumayer, A. Nikroo, J. Nilsen, B. A. Remington, D. Saumon, P. A. Sterne, W. Sweet, A. A. Correa, H. D. Whitley, R. W. Falcone, and S. H. Glenzer, *Nature* **584**, 51 (2020).
- <sup>11</sup>D. Turnbull, A. V. Maximov, D. H. Edgell, W. Seka, R. K. Follett, J. P. Palastro, D. Cao, V. N. Goncharov, C. Stoeckl, and D. H. Froula, *Physical Review Letters* **124**, 185001 (2020).
- <sup>12</sup>D. G. Hicks, N. B. Meezan, E. L. Dewald, A. J. MacKinnon, R. E. Olson, D. A. Callahan, T. Döppner, L. R. Benedetti, D. K. Bradley, P. M. Celliers, D. S. Clark, P. Di Nicola, S. N. Dixit, E. G. Dzenitis, J. E. Eggert, D. R. Farley, J. A. Frenje, S. M. Glenn, S. H. Glenzer, A. V. Hamza, R. F. Heeter, J. P. Holder, N. Izumi, D. H. Kalantar, S. F. Khan, J. L. Kline, J. J. Kroll, G. A. Kyrala, T. Ma, A. G. MacPhee, J. M. McNaney, J. D. Moody, M. J. Moran, B. R. Nathan, A. Nikroo, Y. P. Opachich, R. D. Petrasso, R. R. Prasad, J. E. Ralph, H. F. Robey, H. G. Rinderknecht, J. R. Rygg, J. D. Salmonson, M. B. Schneider, N. Simanovskaia, B. K. Spears, R. Tommasini, K. Widmann, A. B. Zylstra, G. W. Collins, O. L. Landen, J. D. Kilkenny, W. W. Hsing, B. J. MacGowan, L. J. Atherton, and M. J. Edwards, *Physics of Plasmas* **19** (2012), 10.1063/1.4769268.
- <sup>13</sup>J. R. Rygg, O. S. Jones, J. E. Field, M. A. Barrios, L. R. Benedetti, G. W. Collins, D. C. Eder, M. J. Edwards, J. L. Kline, J. J. Kroll, O. L. Landen, T. Ma, A. Pak, J. L. Peterson, K. Raman, R. P. Town, and D. K. Bradley, *Physical Review Letters* **112**, 1 (2014).
- <sup>14</sup>F. J. Marshall, P. W. McKenty, J. A. Delettrez, R. Epstein, J. P. Knauer, V. A. Smalyuk, J. A. Frenje, C. K. Li, R. D. Petrasso, F. H. Séguin, and R. C. Mancini, *Physical Review Letters* **102**, 1 (2009).
- <sup>15</sup>J. Delettrez, R. Epstein, M. C. Richardson, P. A. Jaanimagi, and B. L. Henke, *Physical Review A* **36**, 3926 (1987).
- <sup>16</sup>D. S. Clark, D. E. Hinkel, D. C. Eder, O. S. Jones, S. W. Haan, B. A. Hammel, M. M. Marinak, J. L. Milovich, H. F. Robey, L. J. Suter, and R. P. Town, *Physics of Plasmas* **20** (2013), 10.1063/1.4802194.
- <sup>17</sup>J. L. Peterson, K. D. Humbird, J. E. Field, S. T. Brandon, S. H. Langer, R. C. Nora, B. K. Spears, and P. T. Springer, *Physics of Plasmas* **24** (2017), 10.1063/1.4977912.
- <sup>18</sup>V. Gopalaswamy, R. Betti, J. P. Knauer, N. Luciani, D. Patel, K. M. Woo, A. Bose, I. V. Igumenshchev, E. M. Campbell, K. S. Anderson, K. A. Bauer, M. J. Bonino, D. Cao, A. R. Christopherson, G. W. Collins, T. J. Collins, J. R. Davies, J. A. Delettrez, D. H. Edgell, R. Epstein, C. J. Forrest, D. H. Froula, V. Y. Glebov, V. N. Goncharov, D. R. Harding, S. X. Hu, D. W. Jacobs-Perkins, R. T. Janezic, J. H. Kelly, O. M. Mannion, A. Maximov, F. J. Marshall, D. T. Michel, S. Miller, S. F. Morse, J. Palastro, J. Peebles, P. B. Radha, S. P. Regan, S. Sampat, T. C. Sangster, A. B. Sefkow, W. Seka, R. C. Shah, W. T. Shmyada, A. Shvydky, C. Stoeckl, A. A. Solodov, W. Theobald, J. D. Zuegel, M. G. Johnson, R. D. Petrasso, C. K. Li, and J. A. Frenje, *Nature* **565**, 581 (2019).
- <sup>19</sup>J. A. Gaffney, S. T. Brandon, K. D. Humbird, M. K. Kruse, R. C. Nora, J. L. Peterson, and B. K. Spears, *Physics of Plasmas* **26** (2019), 10.1063/1.5108667.
- <sup>20</sup>J. D. Lindl, P. Amendt, R. L. Berger, S. G. Glendinning, S. H. Glenzer, S. W. Haan, R. L. Kauffman, O. L. Landen, and L. J. Suter, *Physics of Plasmas* **11**, 339 (2004).
- <sup>21</sup>R. S. Craxton, K. S. Anderson, T. R. Boehly, V. N. Goncharov, D. R. Harding, J. P. Knauer, R. L. McCrory, P. W. McKenty, D. D. Meyerhofer, J. F. Myatt, A. J. Schmitt, J. D. Sethian, R. W. Short, S. Skupsky, W. Theobald, W. L. Kruer, K. Tanaka, R. Betti, T. J. Collins, J. A. Delettrez, S. X. Hu, J. A. Marozas, A. V. Maximov, D. T. Michel, P. B. Radha, S. P. Regan, T. C. Sangster, W. Seka, A. A. Solodov, J. M. Soares, C. Stoeckl, and J. D. Zuegel, *Physics of Plasmas* **22**, 0 (2015).
- <sup>22</sup>K. D. Humbird, J. L. Peterson, B. K. Spears, and R. G. McClarren, **48**, 61 (2020).
- <sup>23</sup>J. J. Ruby, J. R. Rygg, J. A. Gaffney, B. Bachmann, and G. W. Collins, *Physics of Fluids* **31** (2019), 10.1063/1.5130769.
- <sup>24</sup>R. Betti, K. Anderson, V. N. Goncharov, R. L. McCrory, D. D. Meyerhofer, S. Skupsky, and R. P. Town, *Physics of Plasmas* **9**, 2277 (2002).
- <sup>25</sup>C. Cerjan, P. T. Springer, and S. M. Sepke, *Physics of Plasmas* **20** (2013), 10.1063/1.4802196.
- <sup>26</sup>P. K. Patel, P. T. Springer, C. R. Weber, L. C. Jarrott, O. A. Hurricane, B. Bachmann, K. L. Baker, L. F. Berzak Hopkins, D. A. Callahan, D. T. Casey, C. J. Cerjan, D. S. Clark, E. L. Dewald, L. Divol, T. Döppner, J. E. Field, D. Fittinghoff, J. Gaffney, V. Geppert-Kleinrath, G. P. Grim,

- E. P. Hartouni, R. Hatarik, D. E. Hinkel, M. Hohenberger, K. Humbird, N. Izumi, O. S. Jones, S. F. Khan, A. L. Kritcher, M. Kruse, O. L. Landen, S. Le Pape, T. Ma, S. A. MacLaren, A. G. MacPhee, L. P. Masse, N. B. Meezan, J. L. Milovich, R. Nora, A. Pak, J. L. Peterson, J. Ralph, H. F. Robey, J. D. Salmonson, V. A. Smalyuk, B. K. Spears, C. A. Thomas, P. L. Volegov, A. Zylstra, and M. J. Edwards, *Physics of Plasmas* **27** (2020), 10.1063/5.0003298.
- <sup>27</sup>E. C. Merritt, J. P. Sauppe, E. N. Loomis, T. Cardenas, D. S. Montgomery, W. S. Daughton, D. C. Wilson, J. L. Kline, S. F. Khan, M. Schoff, M. Hoppe, F. Fierro, R. B. Randolph, B. Patterson, L. Kuettner, R. F. Sacks, E. S. Dodd, W. C. Wan, S. Palaniyappan, S. H. Batha, P. A. Keiter, J. R. Rygg, V. Smalyuk, Y. Ping, and P. Amendt, *Physics of Plasmas* **26** (2019), 10.1063/1.5086674.
- <sup>28</sup>J. R. Rygg, J. A. Frenje, C. K. Li, F. H. Séguin, R. D. Petrasso, D. D. Meyerhofer, and C. Stoeckl, *Physical Review E - Statistical, Nonlinear, and Soft Matter Physics* **80**, 1 (2009).
- <sup>29</sup>L. Spitzer, *Physics of fully ionized gases; 1st ed.*, Internat. Sci. Tracts Phys. Astron. (Interscience, New York, NY, 1956).
- <sup>30</sup>W. Theobald, R. Nora, W. Seka, M. Lafon, K. S. Anderson, M. Hohenberger, F. J. Marshall, D. T. Michel, A. A. Solodov, C. Stoeckl, D. H. Edgell, B. Yaakobi, A. Casner, C. Reverdin, X. Ribeyre, A. Shvydky, A. Vallet, J. Peebles, F. N. Beg, M. S. Wei, and R. Betti, *Physics of Plasmas* **22** (2015), 10.1063/1.4920956.
- <sup>31</sup>B. L. Henke, E. M. Gullikson, and J. C. Davis, *Atomic Data and Nuclear Data Tables* **54**, 181 (1993).
- <sup>32</sup>J. A. Gaffney, D. Clark, V. Sonnad, and S. B. Libby, *Nuclear Fusion* **53** (2013), 10.1088/0029-5515/53/7/073032, arXiv:1302.5745.
- <sup>33</sup>J. A. Gaffney, D. Clark, V. Sonnad, and S. B. Libby, *High Energy Density Physics* **9**, 457 (2013), arXiv:1302.5743.
- <sup>34</sup>L. B. Fletcher, A. L. Kritcher, A. Pak, T. Ma, T. Döppner, C. Fortmann, L. Divol, O. S. Jones, O. L. Landen, H. A. Scott, J. Vorberger, D. A. Chapman, D. O. Gericke, B. A. Mattern, G. T. Seidler, G. Gregori, R. W. Falcone, and S. H. Glenzer, *Physical Review Letters* **112**, 1 (2014).
- <sup>35</sup>S. Atzeni and J. Meyer-Ter-Vehn, *The physics of inertial fusion: beam plasma interaction, hydrodynamics, hot dense matter*, Internat. Mono. Phys. (Clarendon Press, Oxford, 2004).
- <sup>36</sup>R. Betti and O. A. Hurricane, *Nature Physics* **12**, 445 (2016).
- <sup>37</sup>P. T. Springer, O. A. Hurricane, J. H. Hammer, R. Betti, D. A. Callahan, E. M. Campbell, D. T. Casey, C. J. Cerjan, D. Cao, E. Dewald, L. Divol, T. Doeppner, M. J. Edwards, J. E. Field, C. Forrest, J. Frenje, J. A. Gaffney, M. Gatu-Johnson, V. Glebov, V. N. Goncharov, G. P. Grim, E. Hartouni, R. Hatarik, D. E. Hinkel, L. Berzak Hopkins, I. Igumenshchev, P. Knapp, J. P. Knauer, A. L. Kritcher, O. Landen, A. Pak, S. Le Pape, T. Ma, A. G. MacPhee, D. H. Munro, R. C. Nora, P. K. Patel, L. Peterson, P. B. Radha, S. P. Regan, H. Rinderknecht, C. Sangster, B. K. Spears, and C. Stoeckl, *Nuclear Fusion* **59** (2019), 10.1088/1741-4326/aaed65.
- <sup>38</sup>J. J. Ruby, J. R. Rygg, D. A. Chin, J. A. Gaffney, P. J. Adrian, D. Bishel, C. J. Forrest, V. Y. Glebov, N. V. Kabadi, P. M. Nilson, Y. Ping, C. Stoeckl, and G. W. Collins, *Physical Review E* **102**, 53210 (2020).
- <sup>39</sup>J. J. Ruby, J. R. Rygg, D. A. Chin, J. A. Gaffney, P. J. Adrian, C. J. Forrest, V. Y. Glebov, N. V. Kabadi, P. M. Nilson, Y. Ping, C. Stoeckl, and G. W. Collins, *Physical Review Letters* **125**, 215001 (2020).
- <sup>40</sup>J. Colvin and J. Larsen, *Extreme Physics: Properties and Behavior of Matter at Extreme Conditions* (Cambridge University Press, 2013).
- <sup>41</sup>H. S. Bosch and G. M. Hale, *Nuclear Fusion* **32**, 611 (1992).
- <sup>42</sup>J. D. Kilkenny, *Laser and Particle Beams* **9**, 49769 (1991).
- <sup>43</sup>C. Sorce, J. Schein, F. Weber, K. Widmann, K. Campbell, E. Dewald, R. Turner, O. Landen, K. Jacoby, P. Torres, and D. Pellinen, *Review of Scientific Instruments* **77** (2006), 10.1063/1.2336462.
- <sup>44</sup>H. Sio, J. A. Frenje, J. Katz, C. Stoeckl, D. Weiner, M. Bedzyk, V. Glebov, C. Sorce, M. Gatu Johnson, H. G. Rinderknecht, A. B. Zylstra, T. C. Sangster, S. P. Regan, T. Kwan, A. Le, A. N. Simakov, W. T. Taitano, L. Chacón, B. Keenan, R. Shah, G. Sutcliffe, and R. D. Petrasso, *Review of Scientific Instruments* **87** (2016), 10.1063/1.4961552.
- <sup>45</sup>S. F. Khan, L. C. Jarrott, P. K. Patel, N. Izumi, T. Ma, A. G. MacPhee, B. Hatch, O. L. Landen, J. Heinmiller, J. D. Kilkenny, and D. K. Bradley, *Review of Scientific Instruments* **89** (2018), 10.1063/1.5039382.
- <sup>46</sup>V. Y. Glebov, C. Stoeckl, T. C. Sangster, S. Roberts, G. J. Schmid, R. A. Lerche, and M. J. Moran, *Review of Scientific Instruments* **75**, 3559 (2004).
- <sup>47</sup>V. Y. Glebov, T. C. Sangster, C. Stoeckl, J. P. Knauer, W. Theobald, K. L. Marshall, M. J. Shoup, T. Buczek, M. Cruz, T. Duffy, M. Romanofsky, M. Fox, A. Pruyne, M. J. Moran, R. A. Lerche, J. McNaney, J. D. Kilkenny, M. J. Eckart, D. Schneider, D. Munro, W. Stoefl, R. Zacharias, J. J. Haslam, T. Clancy, M. Yeoman, D. Warwas, C. J. Horsfield, J. L. Bourgade, O. Landoa, L. Disdier, G. A. Chandler, and R. J. Leeper, *Review of Scientific Instruments* **81** (2010), 10.1063/1.3492351.
- <sup>48</sup>B. K. Spears, J. Brase, P. T. Bremer, B. Chen, J. Field, J. Gaffney, M. Kruse, S. Langer, K. Lewis, R. Nora, J. L. Peterson, J. Jayaraman Thiagarajan, B. Van Essen, and K. Humbird, *Physics of Plasmas* **25** (2018), 10.1063/1.5020791.
- <sup>49</sup>P. W. Hatfield, S. J. Rose, and R. H. Scott, *Physics of Plasmas* **26** (2019), 10.1063/1.5091985, arXiv:1905.08215.
- <sup>50</sup>M. F. Kasim, T. P. Galligan, J. Topp-Mugglestone, G. Gregori, and S. M. Vinko, *Physics of Plasmas* **26** (2019), 10.1063/1.5125979.
- <sup>51</sup>H. Brysk, *Plasma Physics* **15**, 611 (1973).
- <sup>52</sup>D. H. Munro, *Nuclear Fusion* **56** (2016), 10.1088/0029-5515/56/3/036001.